Check for updates

Borque Paloma (Orcid ID: 0000-0002-3496-3206)

Rugna Martin (Orcid ID: 0000-0001-5258-3162)

Lang Timothy, J (Orcid ID: 0000-0003-1576-572X)

Accepted Article

Distinctive Signals in 1-minute Observations of Overshooting Tops and Lightning Activity in a Severe Supercell Thunderstorm

Paloma Borque[1*], Luciano Vidal[2], Martín Rugna[2], Timothy J. Lang[3], María Gabriela Nicora[4], and Stephen W. Nesbitt[1]

[1]Department of Atmospheric Sciences, University of Illinois at Urbana-Champaign, Urbana, IL, USA

[2]Servicio Meteorológico Nacional, Buenos Aires, Argentina

[3]NASA/Marshall Space Flight Center, Huntsville, AL, USA

[4]CEILAP - UMI-IFAECI-CNRS 3351, UNIDEF (MINDEF - CONICET), Buenos Aires, Argentina

[*]Current affiliation: Pacific Northwest National Laboratory, Richland, WA, USA.

Corresponding author's email: paloma.borque@pnnl.gov

This article has been accepted for publication and undergone full peer review but has not been through the copyediting, typesetting, pagination and proofreading process which may lead to differences between this version and the Version of Record. Please cite this article as doi: 10.1029/2020JD032856

©2020 American Geophysical Union. All rights reserved.

Key Points:

The added value of high-temporal resolution observations of lightning and cloud-top IR is demonstrated for a severe weather event

A possible improvement of lead time for severe weather nowcasting is given by the pulsing behavior of cloud-top brightness temperature

Lifecycle of storms' strong updrafts is likely linked with pulse-like evolution in time of cloud-top brightness temperature minima

Plain Language Summary

Severe thunderstorms can have distinctive signals in satellite observations. Cloud-top temperature minima are one of the most studied metrics as a severe weather indicator. The newest geostationary weather satellites (GOES-16/17) offer a unique opportunity to study storms through their rapid-scan mode and lightning detector. In this study, we analyzed high-temporal (1-min) observations of cloud-top temperature and lightning detected from space and the surface to study the evolution of a severe thunderstorm that took place over central Argentina on December 11, 2018. Overall, cloud-top temperature minimum and fast increases in lightning activity preceded the occurrence of severe weather. The signature present in lightning observations provided the highest severe weather lead time, with ground-based sensors providing the maximum warning time (~30 min). A cloud-top temperature absolute minimum provided the shortest warning time, whereas secondary minima, that preceded the absolute minima, improved the warning time by more than 10 min. This improvement in lead time can result in better societal preparedness for imminent hazardous weather where no ground-based lightning observations are available. Observations with high-temporal resolution also show cycles of fast cloud-top cooling and warming that can provide important insight on the physical processes involved in storm evolution.

©2020 American Geophysical Union. All rights reserved.

Abstract

This work examines a severe weather event that took place over central Argentina on December 11, 2018. The evolution of the storm from its initiation, rapid organization into a supercell, and eventual decay was analyzed with high-temporal resolution observations. This work provides insight into the spatio-temporal co-evolution of storm kinematics (updraft area and lifespan), cloud-top cooling rates, and lightning production that led to severe weather. The analyzed storm presented two convective periods with associated severe weather. An overall decrease in cloud-top local minima IR brightness temperature (MinIR) and lightning jump (LJ) preceded both periods. LJs provided the highest lead time to the occurrence of severe weather, with the ground-based lightning networks providing the maximum warning time of around 30 min. Lightning flash counts from the Geostationary Lightning Mapper (GLM) were underestimated when compared to detections from ground-based lightning networks. Among the possible reasons for GLM's lower detection efficiency were an optically dense medium located above lightning sources and the occurrence of flashes smaller than GLM's footprint. The minimum MinIR provided the shorter warning time to severe weather occurrence. However, the secondary minima in MinIR that preceded the absolute minima improved this warning time by more than 10 min. Trends in MinIR for time scales shorter than 6 min revealed shorter cycles of fast cooling and warming, which provided information about the lifecycle of updrafts within the storm. The advantages of using observations with high-temporal resolution to analyze the evolution and intensity of convective storms are discussed.

Accepted Article

1. Introduction

©2020 American Geophysical Union. All rights reserved.

Deep convective clouds are important to Earth's hydrologic and energy cycles as they strongly affect regional weather and climate (e.g., Stephens 2005). Despite their clear importance, the fundamental mechanisms governing convection initiation, growth, and severe weather production are yet not fully understood. Furthermore, the lifecycle of deep convective systems is inadequately represented in weather and climate models. In particular, timing and location of convective initiation and overall storm evolution are not well characterized in numerical models (Dai 2006; Del Genio et al. 2012; Hagos et al. 2014). This results in low predictability of weather hazards associated with deep convection which has critical social, environmental, and economic implications (e.g., Wallemacq and House 2018 and references therein).

According to several satellite proxies, Southeastern South America (SESA) is known as one of the regions of the world with the most intense and most organized convective systems (Houze et al. 2015; Nesbitt et al. 2006; Velasco and Fritsch 1987; Zipser et al. 2006). SESA is a high lightning flash rate and satellite-estimated hailstorms hotspot and it is where the largest, heaviest rainfall-producing mesoscale convective systems (MCSs) occur (Albrecht et al. 2016; Cecil and Blankenship 2012; Zipser et al. 2006). In particular, MCS-type convection is responsible for the vast majority, by more than 90%, of warm-season precipitation registered over SESA (Houze et al. 2015; Nesbitt et al. 2006; Rasmussen et al. 2014). Storms in this region often develop near complex terrain of the Andes mountain range and Sierras de Córdoba, and produce severe weather hazards such as heavy rainfall that might lead to flash floods, large hail, damaging wind gusts, and tornadoes (Matsudo and Salio 2011; Rasmussen and Houze 2011; Rasmussen et al. 2014). Regional models also struggle to properly represent deep convection in this region (e.g., Carril et al. 2012; Solman et al. 2013). Thus, there is a clear need to improve understanding of the mechanisms involved in convection evolution in this region through in-depth observational studies of such high impact weather events in SESA.

It is important to note that many physical processes involved throughout the life cycle of severe convection are fast-evolving; thus, observations with equally high time resolution are needed (Bedka et al. 2015; Dworak et al. 2012; Mecikalski et al. 2016). Despite their importance, high spatio-temporal radar, surface, and upper-air observations are sparse in most regions, including SESA. However, the RELAMPAGO (Remote sensing of Electrification, Lightning, And Mesoscale/microscale Processes with Adaptive Ground Observations; Nesbitt et al. 2016) – CACTI (Clouds, Aerosols, and Complex Terrain Interactions; Varble et al. 2018)

©2020 American Geophysical Union. All rights reserved.

field campaigns provided such high spatio-temporal observations over central Argentina during Austral summer 2019 (Lang et al. 2020). In particular, Geostationary Operational Environmental Satellite-16 (GOES-16) Mesoscale Domain Sector (MDS) were provided by the National Oceanic and Atmospheric Administration (NOAA) and positioned over central Argentina upon request from the principal investigators of RELAMPAGO-CACTI. Furthermore, in support of these field campaigns, the local sounding network was enhanced by the addition of high-frequency fixed and mobile site launches during intense operational periods (IOPs), and a 3-D Lightning Mapping Array (LMA) operated in Córdoba, central Argentina. All these observations provided an unprecedented dataset in this significant region. More information about the dataset is provided in Section 2.

The availability of the new high-resolution GOES-16/17 satellites presents a unique opportunity to investigate the time evolution of severe weather from a satellite perspective. In particular, this set of observations could revolutionize convection studies in SESA given the clear improvement that it represents to the previously available 10- or 15-min resolution satellite information in the region. Recent studies have analyzed the advantages of super rapid scan operations for GOES and high-temporal lightning observations from ground-based LMAs (Apke et al. 2019; Bedka et al. 2015; Carey et al. 2019; Mecikalski et al. 2016; Ribeiro et al. 2019). Since most physical processes involved throughout the life cycle of severe weather are fast-evolving, it is clear that nowcasting algorithms based on the previously available satellite observations can be improved with state-of-the-art satellite observations. How this improvement is achieved is not trivial. As noted by Bedka et al. (2015), it would be nearly impossible for a forecaster to manually track the evolution of every identified 'threat' in the satellite field when working with 1-min resolution information during an outbreak. Furthermore, given the intrinsic variability present in 1-min observations, the main signals looked for by forecasters in the satellite observations (e.g., fast cloud-top cooling rate) could lead to a significant increase in false alarms when nowcasting severe events (e.g., Ribeiro et al. 2019). The study herein tackles this problem and shows the advantage that 1-min observations represent when capturing the fast-evolving evolution and inherent variability of convective clouds. Observations with such high temporal resolution can provide invaluable insight on storms' dynamics that are not captured by observations with coarse time resolution (lower than 5 min).

©2020 American Geophysical Union. All rights reserved.

This study takes advantage of the vastly enhanced observational network provided by the RELAMPAGO-CACTI field campaigns. In particular, the advantages of using high temporal resolution observations to characterize the evolution of deep convection characteristics (such as cloud top-temperature, lightning activity, hail volume) over a time period exceeding several hours are presented herein. The main goal of this study is to provide insight into the spatio-temporal co-evolution of storms' kinematic structures (updraft area and lifespan), cloud-top cooling rates, and lightning production leading to severe weather occurrence in SESA. For this purpose, observations with high temporal and spatial resolution of an isolated convective cell from its initiation and rapid evolution into a supercell over northeastern Córdoba on December 11, 2018 are studied herein. Additionally, the added value given by combining information provided by different lightning instruments and networks such as the Geostationary Lightning Mapper (GLM), LMA, and Earth Networks Total Lightning Network (ENTLN) is presented. The understanding gained by this analysis is likely to enhance our grasp of the physical processes involved in convective systems globally and can potentially assist in the improvement of its representation in weather and climate models.

2. Datasets

This work examines a case study of severe weather that took place on December 11, 2018 in east-central Córdoba Province in central Argentina during the RELAMPAGO-CACTI field campaigns. RELAMPAGO was a joint project between the U.S., Argentina, and Brazil. During its IOP (from 1 November – 18 December 2018) RELAMPAGO consisted of a suite of fixed and mobile assets that included radars, radiosondes, flux towers, and mobile mesonets that were deployed primarily in Córdoba Province (Fig. 1). From 1 October 2018 to 30 April 2019, CACTI deployed an extensive array of instrumentation, that included the U.S. Department of Energy (DOE) Atmospheric Radiation Measurement (ARM) Mobile Facility and Aerial Facility amongst other ground-based instrumentation. Together, these field campaigns were designed to improve our understanding of severe weather in the region.

During RELAMPAGO-CACTI, the majority of storms developed near the Andes mountain range and Sierras de Córdoba, and many grew upscale into MCS. The severe weather event studied in this work represents the only case of isolated deep convection that initiated in the central plains of Córdoba. MDS, 3-D LMA, and Radar Meteorológico Argentino 1 (RMA1)

©2020 American Geophysical Union. All rights reserved.

observations available during this day captured most of the storm's lifecycle. In particular, all sensors captured convective initiation and supercellular development with high spatio-temporal resolution. Unfortunately, this event occurred outside of the mobile asset domain, and thus it was not sampled by this set of instruments.

2.1 Satellite observations

2.1.1 Advanced Baseline Imager (ABI)

ABI is the primary instrument on the NOAA/NASA GOES-16/17 satellite. ABI is a multi-channel passive imaging radiometer designed to observe Earth with higher temporal, spatial, and radiometric resolution than previous imagers. This instrument has multiple scan modes available with different temporal and spatial resolutions. The mode used during most of RELAMPAGO-CACTI was Mode 3, which provides a Full Disk image every 15 minutes. Also available for these field campaigns was the MDS mode, which provides images every minute with a resolution of 1 km by 1 km at the satellite sub-point. ABI has 16 different spectral bands, two visible channels, four near-infrared channels, and ten infrared channels. Of particular interest to this work, data from 10.3-μm band with 2-km spatial resolution and from the 0.64 -μm band with 0.5-km spatial resolution were used to study the evolution of convective systems in Córdoba Province. Furthermore, from 9 UTC on December 11, 2018 to 3 UTC on December 12, 2018 one MDS was positioned over the RELAMPAGO-CACTI region (Fig. 1) and provided images every minute. Detailed technical information about GOES-16 and the ABI sensor can be found in Schmit et al. (2017).

2.1.2 GLM

GLM is a single-channel, near-infrared optical transient instrument that can detect momentary changes in an optical scene, indicating the presence of lightning. GLM detects total lightning (in-cloud, cloud-to-cloud, and cloud-to-ground) continuously and with a high spatial resolution over the Americas and adjacent ocean regions of approximately 8 km at the satellite sub-point. GLM is the first operational geostationary sensor to measure total lightning activity continuously throughout the day with near-uniform storm-scale spatial resolution with data files produced every 20 seconds. This instrument collects information such as the frequency, location, and extent of lightning discharges via an on-board clustering algorithm. GLM flash counts used herein are from the level 2 product files. More information about GLM can be found in Goodman et al. (2013).

©2020 American Geophysical Union. All rights reserved.

2.2 Ground-based lightning observations

2.2.1 LMA

NASA Marshall Space Flight Center installed an LMA in central Córdoba, Argentina in support of RELAMPAGO from November 2018 to April 2019 (Fig. 1; Lang et al. 2020). This LMA consisted of 11 stations, each with a Very High Frequency (VHF) antenna, receiver, and data processing unit all powered by a solar panel (Fig. 1). The LMA passively detects VHF radiation produced by lightning, and then locates it in 3-D using time-of-arrival techniques originally described by Rison et al. (1999). The LMA provided crucial 3-D, high-resolution, in-cloud observations of intense convection in Argentina during RELAMPAGO-CACTI. The ground-based lightning information provided by the LMA can help our understanding of what processes the GLM observes when lightning occurs in intense convection, especially resolving flashes smaller than the GLM footprint, as well as large, long-lasting stratiform lightning (Rison et al. 1999; Bruning and MacGorman 2013; Lang et al. 2017; Zhang and Cummins 2020).

2.2.2 ENTLN

The ENTLN detects lightning activity using wideband sensors with detection frequencies ranging from 1 Hz to 12 MHz (i.e., from VLF to HF). The ENTLN is deployed in more than 40 countries worldwide with over 50 sensors currently installed in Argentina. In particular, most ENTLN sensors are located in large cities, like Córdoba, thus good coverage and high detection efficiency is expected in the area of study (Fig. 1). ENTLN sensors record electric field waveforms produced by lightning and send the information to a central detection server. Similarly to the LMA, the ENTLN uses time-of-arrival techniques and sophisticated algorithms to determine the 3-D location of each lightning-produced pulse. More information on the ENTLN system can be found in Liu and Heckman (2011).

Flash counts from all lightning sensors were aggregated over a 1-min period and around a 20-km radius from the location of the cloud-top local minima IR brightness temperature (MinIR). The selected 20-km radius was not found to have a major impact on the analysis presented here as the time evolution of flash counts from any of the analyzed sensors does not show a significant variation with distance from MinIR (figure not shown).

2.3 Upper air observations

Upper air observations during RELAMPAGO-CACTI consisted of 6 radiosonde launching sites with a 1-hour to 3-hours launch frequency, depending on the IOP (Servicio

©2020 American Geophysical Union. All rights reserved.

Meteorológico Nacional 2019). Particularly for the event studied here, soundings from Argentina's national meteorological service (SMN; in Spanish) permanent radiosonde station Córdoba Airport (CBA – 31.30°S, 64.21°W) and from RELAMPAGO-CACTI-deployed Villa de María del Río Seco (VMRS – 29.91°S, 63.73°W) station are analyzed (Fig. 1). On December 11, 2018, both of these locations had a 3-hour launch frequency from 9 UTC to 18 UTC followed by hourly launches until 23 UTC.

2.4 Radar observations

RMA1 is a C-band (5.4-cm wavelength), dual-polarization Doppler weather radar located in Córdoba, Argentina (31.44°S, 64.19°W; Fig. 1). This radar was designed and manufactured by INVAP S.E. and is operated by the SMN of Argentina for the National System of Meteorological Radars (SINARAME; in Spanish). The SINARAME project is an Argentine effort to expand the radar network over the entire country. During RELAMPAGO-CACTI, RMA1 performed full Plan Position Indicator (PPI) scans and completed a full volume in 8 min with 450 m range resolution and 0.9° beam width. RMA1 technical information can be found in https://wrd.mgm.gov.tr/Radar/Details/MW1VYmFyTURaSnpFYkl3VXplWjhoZz09. RMA1 data were processed with Python Atmospheric Radiation Measurement (ARM) Radar Toolkit (Py-ART, Helmus and Collis 2016).

3. Methods

3.1 Satellite Observations

ABI dataset was parallax corrected based on cloud-top-height. This is a simple correction that is not expected to affect the validity of the results presented in Section 4 given that the analyzed storm is an isolated system and that a radius of 20-km around MinIR was used to analyze spaceborne with ground-based observations.

3.1.1 Cell Identification and Tracking

Radiation in the GOES-16 10.3 µm channel is unaffected by absorption of atmospheric gases. Therefore, satellite-observed 10.3-µm brightness temperature (IR10.3) can be used as proxy for cloud-top temperature of optically thick clouds (Adler and Mack, 1986). This temperature can also provide information about the intensity of a storm. In particular, the updraft strength can be estimated by the temporal derivative of the IR10.3 (Adler and Fenn,

©2020 American Geophysical Union. All rights reserved.

1979; Mecikalski and Bedka, 2006; Roberts and Rutledge 2003). In general, cloud-top cooling rates greater than 4° in 15 min indicate convective updrafts, while cooling rates of 8° in 15 min are associated with vigorous convective storms preceding strong updrafts (e.g., Mecikalski and Bedka 2006; Roberts and Rutledge 2003). These IR10.3 thresholds are based on previously available 15-min resolution satellite information and should be revisited with the newly available time frequency.

Several objective techniques have been developed for locating storms' cold tops or overshooting tops (OTs) (e.g., Bedka et al. 2012; Vila et al. 2008). In this study, the position and time evolution of storms' coldest tops were determined using a semi-automatic algorithm following three simple steps. First, cell objects were identified in every IR10.3 satellite field as a contiguous region with temperature ≤ 210 K and area > 2 pixels (8 km^2). Second, each IR10.3 local-minima (MinIR) corresponding to the 2.5th percentile of each cell object was selected. This allows to capture all the MinIR associated with the coldest sectors of the storm. Thus, more than one MinIR can be identified within a cell object. Third, each MinIR was manually tracked in time connecting its evolution in subsequent images. This spatio-temporal connection between two consecutive satellite images was determined by the authors, each working independently in order to be as objective as possible (e.g., Bluestein et al. 2019). The resulting MinIR paths were manually checked with the aid of the visible GOES-16 imagery to ensure consistency in the tracks. Tracking in time and space of every detected MinIR provides the ability to analyze the evolution of the intensity (given by changes in brightness temperature and area) of fast-evolving updrafts present within a single storm. In particular, it allows to capture the initiation and decay stages of an updraft before being overpowered by stronger updrafts present in the same storm at the same time.

3.1.2 MinIR Area

Overshooting top area (OTA) has been used as an estimate of updraft width and thus, as proxy for storm intensity (e.g., Marion et al. 2019; Trapp et al. 2017). Marion et al. (2019) developed a technique to estimate OTA by equating the edges of the OT with inflection points in the IR brightness temperature field. For this, they estimate the edge of the OT as the first point where the second derivative in brightness temperature along a radial is negative. Then, assuming a circular OT, the OTA is calculated as OTA = πr^2_m, where r_m is the length of the mean radial calculated over 8 radials. In this work, the area associated with each MinIR (hereafter

©2020 American Geophysical Union. All rights reserved.

referred to as OTA) is estimated following Marion et al. (2019) inflection-based technique but modified to take the identified MinIR as input. Furthermore, the mean radius was calculated over 360 radials - i.e., every 1 degree radially from the MinIR location - to generate a robust OTA estimate.

3.2 Ground-based Radar Observations

3.2.1 Hydrometeor Identification (HID)

HID algorithms using dual-polarimetric radars have been widely used to classify precipitation regions by hydrometeor type (e.g., Bechini and Chandrasekar 2015; Borque et al. 2019; Dolan et al. 2013; Duvernoy and Gaumet 1996; Straka et al. 2000). Particularly, Dolan et al. (2013) C-Band HID algorithm applies fuzzy logic weighting functions to different radar variables (Z_e, differential reflectivity ZDR, specific differential phase KDP, correlation coefficient ρ_{hv}) and environment input (temperature profile) to diagnose 10 different hydrometeor categories (drizzle, rain, wet snow, dry snow, ice crystals, vertically aligned ice, high-density graupel, low-density graupel, hail, and big drops). This algorithm was originally developed for warm-season convection and thus, retrievals of in-storm most probable hydrometeor type at each radar grid point analyzed in this work were estimated following the Dolan et al. (2013) HID algorithm available in the *CSU_RadarTools* open-source software package (https://github.com/CSU-Radarmet/CSU_RadarTools). This algorithm was applied to the dual-polarization RMA1 dataset in polar coordinates and gridded using the nearest neighbor approach onto a 1-km horizontal and vertical resolution grid from surface to 20 km height. KDP was estimated following a finite impulse response (FIR)-based KDP estimation algorithm also available in the *CSU_RadarTools* package and based on Hubbert and Bringi (1995) and Lang et al. (2007) work.

3.2.2 Cell Identification

Storm identification using radar data is an important facet of forecasting the location and strength of severe weather events. Detecting storms and calculating their properties (centroid position, volume, etc.) is an essential part of severe weather warning operations. In addition to providing useful nowcasting capabilities, storm identification and tracking can also provide information suitable for the study of the physical mechanisms of storm evolution (e.g., Dixon and Wiener 1993). In this work, a cell was identified from the radar dataset as a contiguous region with $Z_e \geq 35$ dBZ and area exceeding 25 km^2 (e.g., Roberts and Rutledge

©2020 American Geophysical Union. All rights reserved.

2003). Then, the centroid of each cell was computed following the *scikit-image* image processing toolkit (van der Walt et al. 2014).

3.3 Ground-based Lightning Observations

On December 11, 2018 the LMA had 9 of 11 stations operational. Individual VHF sources were considered in the analysis if their goodness of fit value $\chi^2 \leq 5$ (Rison et al. 1999). Flashes were clustered from individual sources via the Fuchs et al. (2016) algorithm as implemented in the *lmatools* open-source software package (Bruning 2015). Thresholds of no more than 3 km and 150 ms between successive sources within a flash, a maximum possible flash duration of 3 seconds, and a required minimum of 5 sources per flash were used. The first three thresholds are default values commonly used in previous LMA studies, and the last threshold (5 points per flash) was suggested by Lang et al. (2020) as a reasonable threshold for the RELAMPAGO LMA, especially when the lightning array was not operating with the full set of stations. Lang et al. (2020) determined that the RELAMPAGO LMA flash rates were of the highest quality when storms were within 100 km of network center.

Regarding ENTLN, pulses are clustered into a flash following a space (10 km) and time (0.7 s) criteria. ENTLN errors associated with flash location in height are larger than those for latitude and longitude (Liu and Heckman 2011). Thus, given this height uncertainty only flash location in latitude and longitude is analyzed in this work.

4. Case study analysis: December 11, 2018

4.1 Pre-convective Environment

On December 11, 2018 the pre-convective environment over SESA exhibited the typical conditions that lead to the development of severe weather in the region (e.g., Borque et al. 2010; Rasmussen and Houze 2011; Velasco and Fritsch 1987; Vidal 2014). The upper level synoptic flow was characterized by a NW-SE orientated jet-streak centered near 32°S providing high amount of vertical wind shear over central Argentina (Fig. 2a). The leading edge of a 500-hPa trough was located over central Argentina favoring upward motion over the region (Fig. 2b). In the lower levels, the presence of northwestern Argentina low (NAL; Seluchi et al. 2003) and the South American low-level jet (SALLJ) favored warm and moist air advection into central Argentina (Figs. 2c-d). The presence of the SALLJ is further confirmed by the CBA and VMRS sondes (Fig. 3). The 12:00 UTC (9:00 am local time) hodograph from

©2020 American Geophysical Union. All rights reserved.

VMRS shows a very distinct jet-like profile with northerly winds stronger than 22 m s^{-1} around 1.5 km that 4 hours later weakens into a less clear profile (Figs. 3a-b). Further south, the sonde at CBA showed weaker northerly winds in the morning that transitioned to southerly flow by 16:00 UTC (Figs. 3c-d). This suggests the presence of a convergence region in central Córdoba in part as the result of the deceleration at the exit region of the SALLJ over this region. A deep capping inversion is observed from surface to mid-levels of the atmosphere (550/600 hPa) at both sites at 12:00 UTC (Figs. 3a and 3c). This cap, located at the bottom of an elevated mixed layer, prevents deep, moist convection to occur until high values of instability are achieved (e.g., Lanicci and Warner 1991). Previous studies have shown that isolated storms that develop in capped environment tend to occur in areas of enhanced convergence and are likely more severe than widespread storms since there is less competition for available warmth and moisture (Banacos and Ekster 2010; Ribeiro and Bosart 2018). Previous studies have shown that the presence of the NAL in conjunction with the SALLJ is an effective pattern in modulating low-level heat and humidity transport from the tropics into northern-central Argentina that then enhances unstable conditions in the region (e.g., Seluchi and Marengo 2000). Certainly, in the morning of December 11, 2018, the surface-based CAPE was 1008 J kg^{-1} (2900 J kg^{-1}) in CBA (VMRS) at 12:00 UTC and 4 hours later, the instability increased by more than 3000 J kg^{-1} (1000 J kg^{-1}), reaching a value of 4458 J kg^{-1} (4131 J kg^{-1}) by 16:00 UTC (Fig. 3). This increase in instability is also a response to the low-level radiative heating given by clear-sky conditions present in the region (Fig. 2) and to the warm air advection present in the 0-2 km layer given by the counter-clockwise rotation of wind with height in this layer (Fig. 3). Vertical wind shear in the 0–6 km layer in both VMRS and CBA was larger than 10 m s^{-1} at 12:00 UTC and greatly increased towards the afternoon, reaching values higher than 23 m s^{-1} by 16:00 UTC in CBA (Figs. 3a and 3c). Several studies have shown that this amount of vertical wind shear is sufficient to support the development of splitting supercells.

4.2 Convection Evolution

Figure 4 depicts the overall evolution of the convective storms on December 11, 2018 via IR10.3 and Z_e imagery. The storm of interest to this work initiated over east-central Córdoba Province around 16:30 UTC. Cold cloud tops indicating deep convection rapidly intensified and by 17:30 UTC, the storm located around (31.2°S, 63.1°W) registered IR10.3 < -80°C and an anvil thermal couplet (ATC) (Fig. 4a). The low-level reflectivity field from RMA1

©2020 American Geophysical Union. All rights reserved.

hinted at an imminent storm splitting process evident by the pattern of separated 60 dBZ contours. By 17:45 UTC, hail of approximately 3-cm diameter was reported in social media in Carreta Quemada, Córdoba (31.14°S, 63.29°W). Later, by 18:30 UTC the splitting process continued, and two distinct convective cores are evident from the low-level Z_e with IR10.3 < -80°C and an ATC (Fig. 4b). The northern cell, the left mover, centered around (30.9°S, 62.8°W) shows a supercellular structure with hook-echo and V-notch characteristics present in low-level Z_e (Fig. 4b). This is the expected pattern for Southern Hemisphere supercells where the favored cell is the left-mover (equatorward) cell. Around this time, severe weather was reported in several locations of northeastern Córdoba; hail with diameters larger than 5-cm and damage from intense wind gusts were reported in Marull (30.99°S, 62.83°W) and Miramar (30.91°S, 62.7°W) at around 18:40 UTC. Afterwards, storms continued to move eastward with anvils from both convective systems merging with isolated convective cores detected from low-level radar imagery until 20:30 UTC (Fig. 4c). By this time, the cells that are the main focus of this work either dissipated or propagated away from the range of RMA1 and subsequent cells that developed downstream (Fig. 4d) had no severe weather reported and are not analyzed further.

Figure 5 shows the temporal evolution of the storm with the locations of the detected MinIR, the centroid of $Z_e \geq 35$ dBZ at 1 km height, HID-retrieved hail at 1 km and 15 km and lightning from GLM, LMA, and ENTLN. MinIR hint at the splitting process of the storm earlier than the surface radar-observed $Z_e \geq 35$ dBZ centroid (Figs. 5a-b). However, after the splitting process is captured by the 35-dBZ field (after 18:30 UTC) the resulting convective cells presented a more organized and cohesive vertical structure with MinIR nearly collocated with the $Z_e \geq 35$ dBZ centroid (Figs. 5a-b). As expected by the fuzzy-logic weighting functions in the HID algorithm, the 35-dBZ reflectivity contour enclosed the regions where hail is the most probable hydrometeor (Figs. 5c-d). Locations where hail was reported coincides in time and space with regions where hail was the expected hydrometeor type diagnosed by the HID algorithm (Fig. 5c). Furthermore, the cities of Carreta Quemada, Marull, and Miramar are associated with regions where columns of HID-retrieved hail reached heights higher than 15 km (Fig. 5d).

The 35-dBZ contour also enclosed the locations where lightning was detected by GLM, LMA, and ENTLN (Figs. 5e-g). However, LMA and ENTLN detected considerably more flashes

©2020 American Geophysical Union. All rights reserved.

associated with these storms than GLM, especially at the initiation stage, before 18:00 UTC (Figs. 5e-g). While the LMA is capable of detecting lightning flashes beyond 100 km, the detection efficiency is expected to degrade in a manner proportional to distance. Spatial resolution for source locations also degrades beyond 100 km (e.g., Thomas et al. 2004). However, despite the storms' propagation away from this 100-km range limit, the LMA detected more lightning flashes than GLM and a comparable amount to ENTLN as far as 150 km away from the LMA center (Figs. 5e-g). Potential causes for GLM under-detection presented in the literature include: lower GLM detection efficiency at daytime, small LMA flashes at or below the pixel resolution of GLM, multiple LMA flashes manifesting optically at cloud top as a set of pulses that appears to GLM as a single flash, light not reaching cloud top if lightning occurs in or below an optically thick cloud layer (e.g., Fuchs and Rutledge 2018; Light et al. 2001; Thomas et al. 2000). Once the storms moved beyond the range limit of LMA, GLM and ENTLN show comparable results regarding lightning location and timing (quantitative information about this behavior is provided in Section 4.3). However, ENTLN detected more flashes for the left-mover cell, especially after 18:40 UTC (Figs. 5e and 5g).

4.3 Storm Characteristics – Time Series Analysis

The analysis presented in this section is restricted to the portion of the domain that encompasses the track of the left-moving supercell that produced the most significant damage. Figure 6 shows the time evolution of: MinIR, the volume covered with RMA1 observations with $Z_e \geq 35$ dBZ, the area associated with each MinIR, the volume of HID-estimated hail, and flash counts from GLM, LMA, and ENTLN from 16:45 UTC to 20:00 UTC on December 11, 2018. During the analyzed time period, a decrease of MinIR and increase in lightning activity precedes the time of two HID-derived hail cores (Fig. 6). Previous studies have shown that a rapid increase in lightning rate (known as lightning jump (LJ)) is observed before the occurrence of severe weather (Gatlin and Goodman, 2010; Schultz et al. 2011; Schultz et al. 2009; Williams et al. 1999). In this work, LJ is defined following Schultz et al. (2011) 2σ algorithm based on a flash history multi-step methodology for the highest amount of flashes present in the storm as a function of time for each lightning network.

In association with the first HID-derived hail core, hail was reported in social media at Carreta Quemada by 17:45 UTC. Leading to this moment MinIR exhibited its most extreme cooling rate, with an overall decrease of 8.6 °C in 10 min and of -4.1 °C min^{-1} when considering

©2020 American Geophysical Union. All rights reserved.

the 1-min sampling (Fig. 6a). These MinIR cooling rate values suggest the presence of vigorous convective storms. The absolute MinIR of -80 °C occurs at 17:31 UTC representing a 14-min lead time to the occurrence of hail (Fig. 6a). However, a secondary minimum in MinIR of -78 °C took place at 17:22 UTC and thus, considering this minimum improves the lead time by 9 min (Fig. 6a). Both ground-based lightning networks (LMA and ENTLN) detected the LJ associated with this HID-derived hail core at 17:18 UTC (Figs. 6d-e). This time represented the maximum lead time (27 min) for hail occurrence associated with this HID-derived hail core. However, the LJ signal was not captured from GLM observations (Fig. 6c). Prior to 18:20 UTC, when the main storm of interest is within 150 km of the LMA center, LMA and ENTLN detected significantly more – greater than by a factor of 10 – lightning than GLM (Figs. 6c-e). As stated in section 4.2, amongst the possible reasons for GLM's lower detection efficiency are an optically dense medium located above lightning sources that can prevent light from reaching cloud top and flashes smaller than GLM's footprint. Figure 7 shows VHF source density as a function of time and height and the area associated with the flashes detected by LMA and ENTLN. Flash area estimated from LMA and ENTLN shows that lightning flash associated with the detected LJ from these networks were small (area < 40 km^2) (Figs. 7b-c). Given the spatial resolution of GLM, these flashes will most likely not be detected by GLM. In addition to this, before 17:30 UTC the maximum LMA lightning source activity associated with this HID-derived hail core was located at around 10 km height, below the maximum volume of HID-derived hail (centered between 10 km and 12 km height) (Figs. 6b and 7a). Furthermore, RMA1's 8-min time resolution could result in a delayed presence of the HID-derived hail aloft. Therefore, it is not trivial to disentangle the different factors that could have played a role in GLM's under detection for this time.

While the bulk of the lightning occurred below 12 km altitude, the storm also featured significant VHF source activity above 15 km, within the OT (Fig. 7a). OT-based electrical activity has been noted before in the LMA literature (e.g., MacGorman et al. 2017), and similar to those studies, the activity tended to consist of continual low rates of sources without well-defined channels. This may be related to the size of the physical discharges being small relative to the expected spatial resolution of the LMA at ranges like these (~1 km; Thomas et al. 2004). Lang et al. (2020) demonstrated a similar effect (i.e., GLM detecting less lightning during OT periods) in a different storm that also featured OT electrical discharges on

©2020 American Geophysical Union. All rights reserved.

December 14, 2018. The increasing loss in flash source density at low altitude after 18:00 UTC is mostly an LMA effect as the storm moved eastward, away from the LMA-center.

An inverse relationship between MinIR and its associated area (OTA) is present after 18:20 UTC in connection with the second HID-derived hail core (Figs. 6a-b). This suggests that strong updrafts (i.e., updrafts that are capable of generating local minima in satellite-observed brightness temperature) are likely to expand and reach their maximum extent (maximum area) at their most vigorous (coldest MinIR) time (Figs. 6a-b). In particular, between 18:20 UTC and 19:00 UTC the lifecycle of three independent updrafts, as defined by rapid decrease followed by a rapid increase in MinIR, are detected (purple, pink, and grey lines in Figs 6a-b). Each of these updraft intensifications (decrease in MinIR) appeared to be linked with a greater extent of its associated OTA and likewise, the subsequent increase in MinIR was likely linked with an area decrease.

MinIR cooling linked with the second HID-derived hail core was weaker than for the previously described core, with a cooling rate of 1.84 °C min^{-1} (from the 1-min observations) and an overall cooling of almost 6 °C in 10 min that also suggest the presence of vigorous updrafts. However, cooler cloud-top temperatures were present for a longer period of time (MinIR ≤ -85 °C were present for over 5 min from 18:41-18:46 UTC) associated with this HID-derived hail core. The absolute minima of MinIR (-86 °C) occurred at 18:43 UTC, 3 min after hail was reported at Marull and Miramar in Córdoba province (Figs. 6a-b). However, a secondary minimum in MinIR (-80.75 °C) took place at 18:29 UTC thus, representing an 11-min lead time (Fig. 6a). GLM and ENTLN showed higher flash count associated with the second HID-derived hail core and similarly, to the first HID-derived hail core, ENTLN detected more lightning activity than GLM (Figs. 6c and 6e). However, GLM was capable of detecting a LJ at this time (Fig. 6c). ENTLN represented the maximum lead time with the LJ detected at 18:09 UTC (31 min lead time) whereas, GLM's LJ was detected 11 min later, at 18:20 UTC. In association with this LJ, ENTLN detected larger lightning flashes (area > 60 km^2) (Figs. 6c and 7c). Thus, the apparent improvement in GLM detectability was likely associated with the presence of larger lightning flashes. On the other hand, LMA detected fewer flash counts than both GLM and ENTLN, this is most likely due to the range limitations of the LMA as the storm has propagated eastward increasing its distance to the LMA center by more than 150 km (Figs. 5 and 6d). Afterwards, as seen by lightning activity detected by ENTLN and pulses in MinIR,

©2020 American Geophysical Union. All rights reserved.

the storms remained active (Figs. 6a and 6e). By 18:45 UTC the HID-estimated hail core was present at higher altitudes than before (centered at around 10 km height; Fig. 6b). Thus, if the height of the flash source density remained constant or with little variation with time, the denser medium was located at or above the electrical activity source region. This hydrometeor and lightning source configuration could have played a role in GLM's under detection of lightning flashes at this time when ENTLN flash area reached its maximum area of 107.6 km^2 (Figs. 6c, 6e, and 7c). This is consistent with growing evidence that spaceborne sensors like GLM are likely to detect considerably fewer flashes than ground-based networks when the lightning sources are located below an optically thick layer.

4.4 Storm Characteristics – Trends in MinIR

As previously mentioned, the temporal derivative of IR10.3 provides valuable information about the kinematics of the storm, in particular about the updraft strength. Figure 8 shows the temporal evolution of MinIR trends as a function of the temporal interval used to compute these trends (Δt; from 1 min to 10 min). For example, at 17:30 UTC, the top row in each panel in Fig. 8 shows 10-min trends in MinIR (i.e., the difference between MinIR at 17:30 UTC minus MinIR at 17:20 UTC) and similarly, the bottom rows show the 1-min MinIR trend (i.e., the difference between MinIR at 17:30 UTC and MinIR at 17:29 UTC). A cycle of cloud-top cooling and warming surrounding the timing of both HID-derived hail cores (around 17:30 UTC and 18:45 UTC) is evident and present for most time intervals (Fig. 8a). Generally, cloud-top warming is noticeable once the HID-estimated hail volume starts to grow, this is then followed by sharp cooling linked with the moment of maximum amount of hail, that is then followed by intense warming rates possibly linked with updraft decay and hail falling (Fig. 8). However, given RMA1 8-min volume scan resolution, it is challenging to accurately relate rapid changes in MinIR to radar-derived metrics.

The timing of these trends in MinIR depends on the time interval chosen to analyze the evolution of cloud-top temperature. In particular, for the first HID-derived hail core, there is an overall decrease in MinIR for $\Delta t \geq 8$ min with 20 min (17:14 UTC to 17:34 UTC) of consistent cloud-top cooling (Fig. 8b). However, when considering a shorter time interval ($\Delta t \leq 6$ min), this cloud-top cooling period is shortened to 6- or 7-min pulses that are separated by two periods (17:18-17:21 UTC and 17:27-17:30 UTC) of warming cloud tops. Similarly, this pulse-like pattern in MinIR is also present for the second HID-derived hail core but with weaker

©2020 American Geophysical Union. All rights reserved.

cooling and warming rates (Fig. 8c). This pulse-like behavior in warming and cooling cloud-top temperatures is likely showing the lifecycle of the different convective updrafts with a timespan of the order of 5 to 6 minutes. Moreover, between 17:30 UTC and 18:15 UTC, cooling and warming signals of MinIR are disorganized with no clear pattern or pulse-like structure (Fig. 8a). This unorganized behavior in MinIR for all time intervals hints at the collapse of strong updrafts, which is consistent with no severe weather being registered at that time. This ability to infer dynamic characteristics of observed storms, such as the lifecycle of strong updrafts, evidences a clear advantage of the high temporal resolution of satellite observations to improve our understanding of the storms' evolution.

5. Summary and conclusions

This work presents an observational study of an isolated convective event that evolved into a supercell on December 11, 2018 in Córdoba Province, central Argentina. High spatio-temporal observations of cloud-top IR brightness temperature (GOES-16 MDS), lightning counts from ground-based (LMA and ENTLN) and spaceborne (GLM) sensors, and radar reflectivity (RMA1) are analyzed. The overall evolution of the convective storm included convection initiation over east-central Córdoba Province, its rapid intensification, its organization into a supercell, (with cloud-top IR brightness temperature below -80 °C and $Z_e \geq 60$ dBZ), and eventual decay (Figs. 4 and 5).

Consistent with previous studies, an overall decrease in cloud-top local minima IR brightness temperature (MinIR) and increase in lightning activity (lightning jump – LJ) preceded the time of two HID-derived hail cores (Fig. 6). Ground-based sensors (LMA and ENTLN) detected considerably more lightning flashes than the spaceborne sensor (GLM) (Figs. 6c-e). LJs provided the highest lead time to the occurrence of severe weather, with the ground-based networks providing the maximum warning time of around 30 min to the detection of severe weather at surface (Figs. 6b-e). Other LJ did not correspond with severe weather reported at the ground however, given the lack of an official severe weather report network in Argentina and that the storm analyzed in this work developed in a sparsely populated region, it is plausible that severe weather occurred at other times but there is no record of it. The minimum MinIR provided the shorter warning time (Figs. 6a-b). However, secondary minima in MinIR that preceded the absolute minima greatly improved the lead

©2020 American Geophysical Union. All rights reserved.

time to the occurrence of severe weather (Fig. 6). This was the case particularly for the first HID-derived hail core where the secondary minima in MinIR occurred just 4 min after the LJ detected by LMA and ENTLN (Fig. 6). Therefore, tracking the lifecycle of individual minima in cloud-top brightness temperature and not just the overall evolution of a single minimum per storm could represent an improvement in nowcasting by increasing the lead times in the prediction of severe weather. During the second maximum of HID-derived hail, MinIR and its associated area were likely to have an inverse relationship (Figs. 6a-b). This behavior suggests that strong updrafts are prone to expand and reach their maximum extent (area) at their strongest (coldest satellite-observed brightness temperature) time and then decrease in intensity and size as they decay. These findings are clear features in the case analyzed in this work and a statistically robust analyses is needed to validate this approach.

Lightning flash counts were considerably underestimated by GLM, by more than 10 times during much of the analyzed time period, when compared to LMA and ENTLN detections (Figs. 6c-e). Amongst the possible reasons for GLM's lower detection efficiency are an optically dense medium located above lightning sources and flashes smaller than GLM's footprint. This was the case particularly for the first HID-derived hail core where the electrical activity detected by both ground-based sensors consisted of flashes with area < 40 km^2 and the maximum volume of HID-derived hail was located at or above the height of most LMA-detected lightning sources (Figs. 6c-e and 7). Thus, it is not trivial to disentangle the different factors that could have played a role in GLM's under detection at this time. On the other hand, GLM was capable of detecting the LJ associated with the second HID-derived hail core. This apparent improvement in GLM detectability was likely associated with larger lightning flashes present at this time (Figs. 6c and 7c). Therefore, it is important to consider the possible biases in GLM lightning detectability when analyzing storms' characteristics. In particular, if GLM is the only sensor available to assess the strength of the storm, then this deficiency in GLM detection efficiency can potentially impact forecasters' decisions when heavily relying on GLM as a nowcasting tool. However, when ground-based lightning sensors are also available, this GLM 'weakness' could be leveraged into an advantage to infer that a considerable amount of hydrometeors able to extinct, or considerably diminish, flash radiation (like graupel and/or hail) is likely present in the storm and it can then provide important knowledge of the severity

©2020 American Geophysical Union. All rights reserved.

of the storm. It is possible that rapidly cooling or wide OTs could signal the potential development of GLM under detection and signal the severity of a storm.

Trends in MinIR over a time period of tens of minutes shows an overall cooling preceding the occurrence of severe weather. However, trends in MinIR for time scales shorter than 5 or 6 min reveal a shorter pulse-like cycle of fast cooling and warming (Fig. 8). This pulse-like behavior in MinIR trends have a consistent structure throughout different time intervals used to compute the temperature trends and hints at a longer lead time for severe weather prediction given by observations with high temporal resolution when looking at MinIR trends at a particular time interval. Furthermore, trends in MinIR with time resolution finer than 2 min are likely too noisy and will lead to false alarms being issued when used exclusively as a severe weather indicator. However, 1-min MDS scans allows the computation of cooling and warming trends every minute at different time intervals, and thus enable consistency in the warming and cooling signals at the different time intervals. Consistent trends in MinIR are likely to result in quantitative information that can be used to increase lead times while reducing false alarms when nowcasting severe weather occurrence. Moreover, this pulse-like structure in cooling and warming trends in MinIR is likely linked to updraft activity, and the period of these pulses hints at the duration of the strong updrafts present in the storm. The ability to infer dynamics of observed convection, such as the lifecycle of strong updrafts, advances our understanding of the storms' evolution that should culminate with an improvement of models' representation of convection lifecycle. These fast-evolving cooling and warming signatures could be analyzed in more detail with high resolution modeling studies capable of representing the storms' dynamics providing enhanced knowledge of storms' dynamics. It is important to note that the pulsing behavior in MinIR is smoothed to an almost indistinguishable signal when analyzing observations with coarser time resolution (lower than 6 or 7 min).

This work demonstrates the need for more studies of severe weather events using observations with high spatio-temporal resolution. Such studies should help confirm whether the patterns seen in this work are consistent throughout a larger convective dataset. The extensive MDS dataset collected in RELAMPAGO-CACTI field campaigns could advance our understanding of storms' evolution in one of the regions of the world with the most intense convection. The examination of additional cases could help address how GLM and ABI

©2020 American Geophysical Union. All rights reserved.

Accepted Article

measurements can be used to understand convective processes, including the uniqueness of storms in SESA. Furthermore, given the increasing availability of ground-based LMAs in other parts of the world, ground-based radar networks, as well as the continuously increasing dataset from GOES-16 MDS, synergistic studies (including an independent corroboration of updraft lifecycle given by multi-Doppler retrievals) could also represent a significant improvement in our understanding of the dynamics involved in continental deep convection.

Acknowledgments

This research was supported by the National Science Foundation through Grant AGS-1661719. Additional funding for this study was provided by the U.S. Department of Energy Office of Science Biological and Environmental Research as part of the Atmospheric System Research Program. Pacific Northwest National Laboratory is operated by Battelle for the U.S. department of Energy under Contract DE-AC05-76RLO1830. RELAMPAGO was funded in Argentina by the SMN and the Province of Córdoba, and in the USA by the NSF, NASA, and NOAA. CACTI was a U.S. DOE-ARM funded project. Funding for the RELAMPAGO LMA came from the NOAA GOES-R Program, with additional support from the NASA Lightning Imaging Sensor (LIS) project. LMA data are available from NASA (http://dx.doi.org/10.5067/RELAMPAGO/LMA/DATA101). Data provided by NCAR/EOL under the sponsorship of the National Science Foundation. RMA1 data was provided by Secretaría de Infraestructura y Política Hídrica, Ministerio del Interior, Obras Públicas y Vivienda of the Argentine National Government framed within the Sistema Nacional de Radares Meteorológicos (SINARAME) Project. The authors thank three anonymous reviewers for their helpful comments and suggestions that helped improve the manuscript, Steven Goodman for his support in providing MDS over the RELAMPAGO-CACTI area, and Earth Networks for providing the lightning data (https://www.earthnetworks.com/why-us/networks/lightning/), which can be obtained by contacting Steve Prinzivalli (sprinzivalli@earthnetworks.com).

Accepted Article

©2020 American Geophysical Union. All rights reserved.

REFERENCES

Adler, R.F. and D.D. Fenn, 1979: Thunderstorm Intensity as Determined from Satellite Data. *J. Appl. Meteor.*, **18**, 502–517, https://doi.org/10.1175/1520-0450(1979)018<0502:TIADFS>2.0.CO;2

Adler, R. F., and R. A. Mack, 1986: Thunderstorm cloud top dynamics as inferred from satellite observations and a cloud top parcel model. *J. Atmos. Sci.*, **43**, 1945–1960

Albrecht, R.I., S.J. Goodman, D.E. Buechler, R.J. Blakeslee, and H.J. Christian, 2016: Where Are the Lightning Hotspots on Earth?. *Bull. Amer. Meteor. Soc*., **97**, 2051–2068, https://doi.org/10.1175/BAMS-D-14-00193.1

Apke, J.M., J.R. Mecikalski, K. Bedka, E.W. McCaul, C.R. Homeyer, and C.P. Jewett, 2018: Relationships between Deep Convection Updraft Characteristics and Satellite-Based Super Rapid Scan Mesoscale Atmospheric Motion Vector–Derived Flow. *Mon. Wea. Rev.,* **146**, 3461–3480, https://doi.org/10.1175/MWR-D-18-0119.1

Banacos, P. C., and M. L. Ekster, 2010: The association of the elevated mixed layer with significant severe weather events in the northeastern United States. Wea. Forecasting, 25, 1082–1102, https://doi.org/10.1175/2010WAF2222363.1

Bechini, R. and V. Chandrasekar, 2015: A Semisupervised Robust Hydrometeor Classification Method for Dual-Polarization Radar Applications. *J. Atmos. Oceanic Technol.*, **32**, 22–47, https://doi.org/10.1175/JTECH-D-14-00097.1

Bedka, K.M., R. Dworak, J. Brunner, and W. Feltz, 2012: Validation of Satellite-Based Objective Overshooting Cloud-Top Detection Methods Using CloudSat Cloud Profiling Radar Observations. *J. Appl. Meteor. Climatol.*, **51**, 1811–1822, https://doi.org/10.1175/JAMC-D-11-0131.1

Bedka, K. M., C. Wang, R. Rogers, L. D. Carey, W. Feltz, and J. Kanak, 2015: Examining deep convective cloud evolution using total lightning, WSR-88D, and *GOES-14* super rapid scan datasets. *Wea. Forecasting*, **30**, 571–590, https://doi.org/10.1175/WAF-D-14-00062.1

Bluestein, H.B., D.T. Lindsey, D. Bikos, D.W. Reif, and Z.B. Wienhoff, 2019: The Relationship between Overshooting Tops in a Tornadic Supercell and Its Radar-Observed Evolution. *Mon. Wea. Rev.*, **147**, 4151–4176, https://doi.org/10.1175/MWR-D-19-0159.1

Borque, P., S.W. Nesbitt, R.J. Trapp, S. Lasher-Trapp, and M. Oue, 2020: Observational study of the thermodynamics and morphological characteristics of a midlatitude continental cold pool event. *Mon. Wea. Rev.*, **0**, https://doi.org/10.1175/MWR-D-19-0068.1

Accepted Article

©2020 American Geophysical Union. All rights reserved.

Borque, P., P.Salio, M.Nicolini, and Y.García Skabar, 2010: Environment associated with deep moist convection under SALLJ conditions: A case study. *Wea. Forecasting*, **25**, 970–984, doi:https://doi.org/10.1175/2010WAF2222352.1.

Bruning, E.C. and D.R. MacGorman, 2013: Theory and Observations of Controls on Lightning Flash Size Spectra. J. Atmos. Sci., 70, 4012-4029, https://doi.org/10.1175/JAS-D-12-0289.1

Bruning, E. C., 2015: lmatools: Python code for working with VHF Lightning Mapping Array data. DOI: 10.5281/zenodo.32510

Carey, L.D.; Schultz, E.V.; Schultz, C.J.; Deierling, W.; Petersen, W.A.; Bain, A.L.; Pickering, K.E. An Evaluation of Relationships between Radar-Inferred Kinematic and Microphysical Parameters and Lightning Flash Rates in Alabama Storms. *Atmosphere* **2019**, *10*, 796.

Carril, AF, CG Menendez, ARC Remedio, F Robledo, A Sorensson, B Tencer, J-P Boulanger, M d Castro, D Jacob, H Le Truet, LZX Li, O Penalba, S Pfeifer, M Rusticucci, P Salio, P Samuelsson, E Sanchez, and P Zaninelli, 2012. "Performance of a multi-RCM ensemble for South Eastern South America. *Climate Dynamics,* **39**: 2747–2768, https://doi.org/10.1007/s00382-012-1573-z

Cecil, D.J., 2009: Passive Microwave Brightness Temperatures as Proxies for Hailstorms. *J. Appl. Meteor. Climatol.,* **48**, 1281–1286, https://doi.org/10.1175/2009JAMC2125.1

Cecil, D.J. and C.B. Blankenship, 2012: Toward a Global Climatology of Severe Hailstorms as Estimated by Satellite Passive Microwave Imagers. *J. Climate,* **25**, 687–703, https://doi.org/10.1175/JCLI-D-11-00130.1

Cifelli, R., V. Chandrasekar, S. Lim, P.C. Kennedy, Y. Wang, and S.A. Rutledge, 2011: A New Dual-Polarization Radar Rainfall Algorithm: Application in Colorado Precipitation Events. J. *Atmos. Oceanic Technol.*, **28**, 352–364, https://doi.org/10.1175/2010JTECHA1488.1

Cordeira, J. M., N. D. Metz, M. E. Howarth, and T. J. Galarneau Jr., 2017: Multiscale upstream and in situ precursors to the elevated mixed layer and high-impact weather over the Midwest United States. *Wea. Forecasting*, 32, 905–923, https://doi.org/10.1175/WAF-D-16-0122.1

Dai, A., 2006: Precipitation Characteristics in Eighteen Coupled Climate Models. *J. Climate,* **19**, 4605–4630, https://doi.org/10.1175/JCLI3884.1

Del Genio, AD, J Wu, and Y Chen. 2012. Characteristics of mesoscale organization in WRF simulations of convection during TWP-ICE. *Journal of Climate* 25(17): 5666–5688, https://doi.org/10.1175/JCLI-D-11-00422.1

Dixon, M. and G. Wiener, 1993: TITAN: Thunderstorm Identification, Tracking, Analysis, and Nowcasting—A Radar-based Methodology. *J. Atmos. Oceanic Technol.*, **10**, 785–797, https://doi.org/10.1175/1520-0426(1993)010<0785:TTITAA>2.0.CO;2

©2020 American Geophysical Union. All rights reserved.

Dolan, B., S.A. Rutledge, S. Lim, V. Chandrasekar, and M. Thurai, 2013: A Robust C-Band Hydrometeor Identification Algorithm and Application to a Long-Term Polarimetric Radar Dataset. *J. Appl. Meteor. Climatol.*, **52**, 2162–2186, https://doi.org/10.1175/JAMC-D-12-0275.1

Duvernoy, J. and J.L. Gaumet, 1996: Precipitating Hydrometeor Characterization by a CW Doppler Radar. *J. Atmos. Oceanic Technol*., **13**, 620–629, https://doi.org/10.1175/1520-0426(1996)013<0620:PHCBAC>2.0.CO;2

Dworak, R., K. Bedka, J. Brunner, and W. Feltz, 2012: Comparison between GOES-12 Overshooting-Top Detections, WSR-88D Radar Reflectivity, and Severe Storm Reports. *Wea. Forecasting,* **27**, 684–699, https://doi.org/10.1175/WAF-D-11-00070.1

Fuchs, B. R., & Rutledge, S. A. (2018): Investigation of lightning flash locations in isolated convection using LMA observations. JGR: Atmospheres, **123**, 6158–6174. https://doi.org/10.1002/2017JD027569

Fuchs, B. R., E. C., Bruning, S. A., Rutledge, L. D., Carey, P. R., Krehbiel, and W. Rison, 2016: Climatological analyses of LMA data with an open-source lightning clustering algorithm. *J. Geophys. Res.,* **121**, 8625-8648. https://doi.org/10.1002/2015JD024663

Gatlin, P.N. and S.J. Goodman, 2010: A Total Lightning Trending Algorithm to Identify Severe Thunderstorms. *J. Atmos. Oceanic Technol.,* **27**, 3–22, https://doi.org/10.1175/2009JTECHA1286.1

Goodman, S. J., et al. 2013: The GOES-R Geostationary Lightning Mapper (GLM). *J. Atmos. Res.*, **125–126**, 34–49. https://doi.org/10.1016/j.atmosres.2013.01.006

Hagos, S, Z Feng, CD Burleyson, K-S S Lim, CN Long, D Wu, and G Thompson. 2014. Evaluation of convection-permitting model simulations of cloud populations associated with the Madden-Julian Oscillation using data collected during the AMIE/DYNAMO field campaign. *Journal of Geophysical Research – Atmospheres* 119(21): 12,052–12,068, https://doi.org/10.1002/2014JD022143

Helmus, J. J., and S. M. Collis, 2016: The Python ARM Radar Toolkit (Py-ART), a library for working with weather radar data in the Python programming language. *J. Open Res. Software*, **4**, e25, https://doi.org/10.5334/jors.119.

Hohenegger, C, and B Stevens. 2013. Preconditioning deep convection with cumulus congestus. *Journal of the Atmospheric Sciences* 70(2): 448–464, https://doi.org/10.1175/JAS-D-12-089.1

Houze, R. A. Jr., Rasmussen, K. L., Zuluaga, M. D., and Brodzik, S. R. (2015). The variable nature of convection in the tropics and subtropics: A legacy of 16 years of the Tropical Rainfall Measuring Mission satellite. *Reviews of Geophysics*, **53**, 994–1021. https://doi.org/10.1002/2015RG000488

©2020 American Geophysical Union. All rights reserved.

Hubbert, J. and V.N. Bringi, 1995: An Iterative Filtering Technique for the Analysis of Copolar Differential Phase and Dual-Frequency Radar Measurements. *J. Atmos. Oceanic Technol.,* **12**, 643–648, https://doi.org/10.1175/1520-0426(1995)012<0643:AIFTFT>2.0.CO;2

Lang, T. J., D. A. Ahijevych, S. W. Nesbitt, R. E. Carbone, S. A. Rutledge, and R. Cifelli, 2007: Radar-Observed Characteristics of Precipitating Systems during NAME 2004. *J. Climate*, **20**, 1713–1733. doi: http://dx.doi.org/10.1175/JCLI4082.1

Lang, T. J., et al., 2017: WMO World Record Lightning Extremes: Longest Detected Flash Distance and Longest Detected Flash Duration. *Bull. Amer. Meteor. Soc.*, **98**, doi: 10.1175/BAMS-D-16-0061.1.

Lang, T. J., and Coauthors, The RELAMPAGO Lightning Mapping Array, 2020: Overview and initial comparison to the Geostationary Lightning Mapper. *J. Atmos. Oceanic Technol.*, doi: https://doi.org/10.1175/JTECH-D-20-0005.1

Lanicci, J.M. and T.T. Warner, 1991: A Synoptic Climatology of the Elevated Mixed-Layer Inversion over the Southern Great Plains in Spring. Part I: Structure, Dynamics, and Seasonal Evolution. *Wea. Forecasting,* **6**, 181–197 https://doi.org/10.1175/1520-0434(1991)006<0181:ASCOTE>2.0.CO;2

Light, T., Suszcynsky, D., Kirkland, M., & Jacobson, A. (2001). Simulations of lightning optical waveforms as seen through clouds by satellites. *Journal of Geophysical Research*, **106**(D15), 17,103–17,114. https://doi.org/10.1029/2001JD900051

Liu, H., and V. Chandrasekar, 2000: Classification of hydrometeors based on polarimetric radar measurements: Development of fuzzy logic and neuro-fuzzy systems, and in situ verification. J. Atmos. Oceanic Technol., 17, 140–164, https://doi.org/10.1175/1520-0426(2000)017,0140: COHBOP.2.0.CO;2.

Liu, C., and Heckman, S. (2011). The application of total lightning detection and cell tracking for severe weather prediction. In *91st American Meteorological Society Annual Meeting*, Seattle.

MacGorman, D. R., M. S. Elliott, and E. DiGangi, 2017: Electrical discharges in the overshooting tops of thunderstorms, *J. Geophys. Res. Atmos.*, **122**, 2929–2957, doi:10.1002/2016JD025933.

Marion, G.R., R. J. Trapp, and S. W. Nesbitt, 2019: Using Overshooting Top Area to Discriminate Potential for Large, Intense Tornadoes. *Geophys. Res. Lett.,* **46**, 12520-12526, https://doi.org/10.1029/2019GL084099

Matsudo, C. y Salio, P. V. (2011). Severe weather reports and proximity to deep convection over Northern Argentina. Atmospheric Research, 100(4):523-537.

Mecikalski, J.R. and K.M. Bedka, 2006: Forecasting Convective Initiation by Monitoring the Evolution of Moving Cumulus in Daytime GOES Imagery. *Mon. Wea. Rev.*, **134**, 49–78, https://doi.org/10.1175/MWR3062.1

©2020 American Geophysical Union. All rights reserved.

Mecikalski, J. R., C. P. Jewett, J. M. Apke, and L. D. Carey, 2016: Analysis of cumulus cloud updrafts as observed with 1-min resolution Super Rapid Scan GOES imagery. *Mon. Wea. Rev.*, **144**, 811–830, https://doi.org/10.1175/MWR-D-14-00399.1

Mezher, Romina & Doyle, M. and Barros, V. (2012). Climatology of hail in Argentina. Atmospheric Research. s 114–115. 70–82. 10.1016/j.atmosres.2012.05.020.

Nesbitt, S.W., R. Cifelli, and S.A. Rutledge, 2006: Storm Morphology and Rainfall Characteristics of TRMM Precipitation Features. *Mon. Wea. Rev.,* **134**, 2702–2721, https://doi.org/10.1175/MWR3200.1

Nesbitt, S. W., and co-authors, 2016: RELAMPAGO Experimental Design Overview. 59 pp, https://www.eol.ucar.edu/field_projects/relampago

Ni, X., C. Liu, and E. Zipser, 2019: Ice Microphysical Properties near the Tops of Deep Convective Cores Implied by the GPM Dual-Frequency Radar Observations. *J. Atmos. Sci.,* **76**, 2899–2917, https://doi.org/10.1175/JAS-D-18-0243.1

Rasmussen, KL, and RA Houze, Jr. 2011. Orogenic convection in South America as seen by the TRMM satellite. *Monthly Weather Review* 139(8): 2399–2420, https://doi.org/10.1175/MWR-D-10-05006.1

Rasmussen, K. L., M. D. Zuluaga, and R. A. Houze, 2014: Severe convection and lightning in subtropical South America. *Geophys. Res. Lett.*, **41**, 7359–7366, https://doi.org/10.1002/2014GL061767

Rasmussen, K.L. and R.A. Houze, 2016: Convective Initiation near the Andes in Subtropical South America. Mon. Wea. Rev.,144, 2351–2374, https://doi.org/10.1175/MWR-D-15-0058.1

Ribeiro, B.Z. and L.F. Bosart, 2018: Elevated Mixed Layers and Associated Severe Thunderstorm Environments in South and North America. Mon. Wea. Rev., 146,3–28, https://doi.org/10.1175/MWR-D-17-0121.1

Ribeiro, B.Z., L.A. Machado, J.H. Huamán Ch., T.S. Biscaro, E.D. Freitas, K.W. Mozer, and S.J. Goodman, 2019: An Evaluation of the GOES-16 Rapid Scan for Nowcasting in Southeastern Brazil: Analysis of a Severe Hailstorm Case. *Wea. Forecasting,* **34**, 1829–1848, https://doi.org/10.1175/WAF-D-19-0070.1

Rison, W., R. Thomas, P. Krehbiel, T. Hamlin, and J. Harlin, 1999: A GPS-based three-dimensional lightning mapping system: Initial observations in central New Mexico, *Geophys. Res. Lett*., **26**, 3573-3576.

Roberts, R.D. and S. Rutledge, 2003: Nowcasting Storm Initiation and Growth Using GOES-8 and WSR-88D Data. *Wea. Forecasting*, **18**, 562–584, https://doi.org/10.1175/1520-0434(2003)018<0562:NSIAGU>2.0.CO;2

©2020 American Geophysical Union. All rights reserved.

Ryzhkov, A. V., T. J. Schuur, D. W. Burgess, P. L. Heinselman, S. E. Giangrande, and D. S. Zrnic´, 2005: The Joint Polarization Experiment: Polarimetric rainfall measurements and hydrometeor classification. *Bull. Amer. Meteor. Soc.*, **86**, 809–824, doi:10.1175/BAMS-86-6-809

Schmit, T. J., P. Griffith, M. M. Gunshor, J. M. Daniels, S. J. Goodman, and W. J. Lebair, 2017: A Closer Look at the ABI on the GOES-R Series. *Bull. Amer. Meteor. Soc.*, **98**, 681–698, https://doi.org/10.1175/BAMS-D-15-00230.1

Schultz, C.J., W.A. Petersen, and L.D. Carey, 2011: Lightning and Severe Weather: A Comparison between Total and Cloud-to-Ground Lightning Trends. Wea. Forecasting, 26, 744–755, https://doi.org/10.1175/WAF-D-10-05026.1

Schultz, C.J., W.A. Petersen, and L.D. Carey, 2009: Preliminary Development and Evaluation of Lightning Jump Algorithms for the Real-Time Detection of Severe Weather. J. Appl. Meteor. Climatol., 48, 2543–2563, https://doi.org/10.1175/2009JAMC2237.1

Seluchi, M. E., A. C. Saulo, M. Nicolini, and P. Satyamurty, 2003: The Northwestern Argentinean Low: A Study of Two Typical Events. *Mon. Wea. Rev.*, **131**, 2361–2378, https://doi.org/10.1175/1520-0493(2003)131<2361:TNALAS>2.0.CO;2

Seluchi, M. E., and J. A. Marengo, 2000: Tropical–midlatitude exchange of air masses during summer and winter in South America: Climatic aspects and examples of intense events. *Int. J. Climatol.*, **20**, 1167–1190, https://doi.org/10.1002/1097-0088(200008)20:10<1167::AID-JOC526>3.0.CO;2-T.

Servicio Meteorológico Nacional, 2019: SMN Radiosonde Data. Version 1.0. UCAR/NCAR - Earth Observing Laboratory. https://doi.org/10.26023/E8MP-0GD3-4903. Accessed 25 Sep 2019.

Solman, S.A., Blázquez, J. Multiscale precipitation variability over South America: Analysis of the added value of CORDEX RCM simulations. Clim Dyn 53, 1547–1565 (2019). https://doi.org/10.1007/s00382-019-04689-1

Solman, SA, E Sanchez, P Samuelsson, R.P. da Rocha, L Li, J Marengo, NL Pessacg, ARC Remedio, SC Chou, H Berbery, H Le Treut, M de Castro and D Jacob. 2013. Evaluation of an ensemble regional climate model simulations over South America driven by the ERA-Interim reanalyses: model performance and uncertainties. *Climate Dynamics* 41(5-6): 1139–1157, https://doi.org/10.1007/s00382-013-1667-2

Song, H, W Lin, Y Lin, AB Wolf, R Neggers, LJ Donner, AD Del Genio, and Y Liu. 2013. Evaluation of precipitation simulated by seven SCMs against the ARM observations at the SGP site. *Journal of Climate* **26**: 5467–5492, https://doi.org/10.1175/JCLI-D-12-00263.1

Steiger, S. M., R. E. Orville, M. J. Murphy, and N. W. S. Demetriades, 2005: Total lightning and radar characteristics of supercells: Insights on electrification and severe weather forecasting.

©2020 American Geophysical Union. All rights reserved.

Preprints, Conf. on the Meteorological Application of Lightning Data, San Diego, CA, Amer. Meteor. Soc., P1.7. [Available online at http://ams.confex.com/ams/pdfpapers/84908.pdf

Stephens, G.L., 2005: Cloud Feedbacks in the Climate System: A Critical Review. *J. Climate,* **18**, 237–273, https://doi.org/10.1175/JCLI-3243.1

Straka, J. M., and D. S. Zrnić, and A. V. Ryzhkov, 2000: Bulk hydrometeor classification and quantification using polarimetric radar data: Synthesis of relations. *J. Appl. Meteor.*, **39**, 1341–1372, doi:10.1175/1520-0450(2000)039,1341:BHCAQU.2.0.CO;2.

Thomas, R. J., Krehbiel, P. R., Rison, W., Hunyady, S. J., Winn, W. P., Hamlin, T., & Harlin, J. (2004). Accuracy of the lightning mapping array. *J. Geophys. Res.*, **109**, D14207. https://doi.org/10.1029/2004JD004549

Thomas, R. J., Krehbiel, P. R., Rison, W., Hamlin, T., Boccippio, D. J., Goodman, S. J., & Christian, H. J. (2000). Comparison of ground-based 3-dimensional lightning mapping observations with satellite-based LIS observations in Oklahoma. *Geophysical Research Letters*, **27**(12), 1703–1706. https://doi.org/10.1029/1999GL010845

Trapp, R. J., Marion, G. R., & Nesbitt, S. W. (2017). The regulation of tornado intensity by updraft width. *J. Atmos. Sci.*, **74**, 4199–4211. https://doi.org/10.1175/JAS-D-16-0331.1

van der Walt S., J. L. Schönberger, J. Nunez-Iglesias, F. Boulogne, J. D. Warner, N. Yager, E. Gouillart, T. Yu, and the scikit-image contributors, 2014: scikit-image: Image processing in Python. *PeerJ* 2:e453 https://doi.org/10.7717/peerj.453

Varble, A., and co-authors, 2018: Cloud, Aerosol, and Complex Terrain Interactions (CACTI) Science Plan. DOE/ARM Technical Report# DOE/SC-ARM-17-004. 48 pp, https://www.arm.gov/research/campaigns/amf2018cacti

Velasco, I., and J. M. Fritsch, 1987: Mesoscale convective complexes in the Americas. *J. Geophys. Res.*, **92**, 9591–9613, doi:https://doi.org/10.1029/JD092iD08p09591

Vidal, L., 2014: Convección extrema sobre Sudamérica: estructura interna, ciclos de vida e influencia de la topografía en la iniciación. Tesis doctoral, Facultad de Ciencias Exactas y Naturales. Universidad de Buenos Aires.

Vila, D. A., L. A. T. Machado, H. Laurent, and I. Velasco, 2008: Forecast and Tracking the Evolution of Cloud Clusters (ForTraCC) using satellite infrared imagery: Methodology and validation. *Wea. Forecasting*, **23**, 233–245, doi:https://doi.org/10.1175/2007WAF2006121.1

Wallemacq, P., and House R., 2018: Economic losses, poverty & disasters: 1998-2017. Centre for Research on the Epidemiology of Disasters United Nations Office for Disaster Risk Reduction. This document is available on https://www.preventionweb.net/files/61119_credeconomiclosses.pdf

©2020 American Geophysical Union. All rights reserved.

Williams, E., Boldi, B., Matlin, A., Weber, M., Hodanish, S., Sharp, D., … Buechler, D. (1999). The behavior of total lightning activity in severe Florida thunderstorms. *Atmospheric Research*, **51**(3-4), 245–265. https://doi.org/10.1016/S0169-8095(99)00011-3

Zhang, D., and Cummins, K. L. (2020): Time evolution of satellite-based optical properties in lightning flashes, and its impact on GLM flash detection. JGR: Atmospheres, **125**, e2019JD032024. https://doi.org/10.1029/2019JD032024

Zipser, EJ, DJ Cecil, C Liu, SW Nesbitt, and DP Yorty. 2006. "Where are the most intense thunderstorms on Earth?" *Bulletin of the American Meteorological Society* 87(8): 1057–1071, https://doi.org/10.1175/BAMS-87-8-1057

Accepted Article

©2020 American Geophysical Union. All rights reserved.

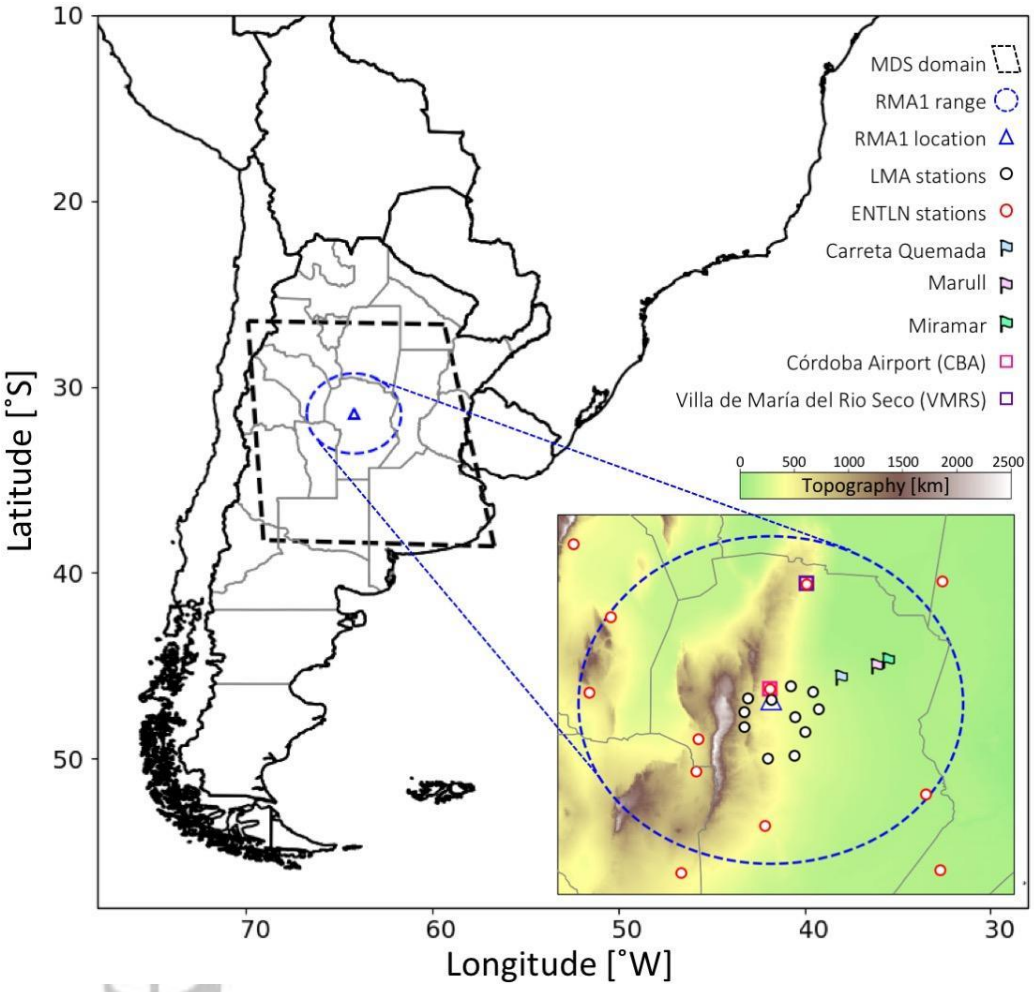

Fig. 1: Map of the study region with location of the RMA1 radar (triangle), its radius of influence (dashed blue circle), MDS domain (dashed black line), LMA stations (black circles), ENTLN stations (red circles), sondes stations (squares), and locations where severe weather was reported (flags).

Accepted

©2020 American Geophysical Union. All rights reserved.

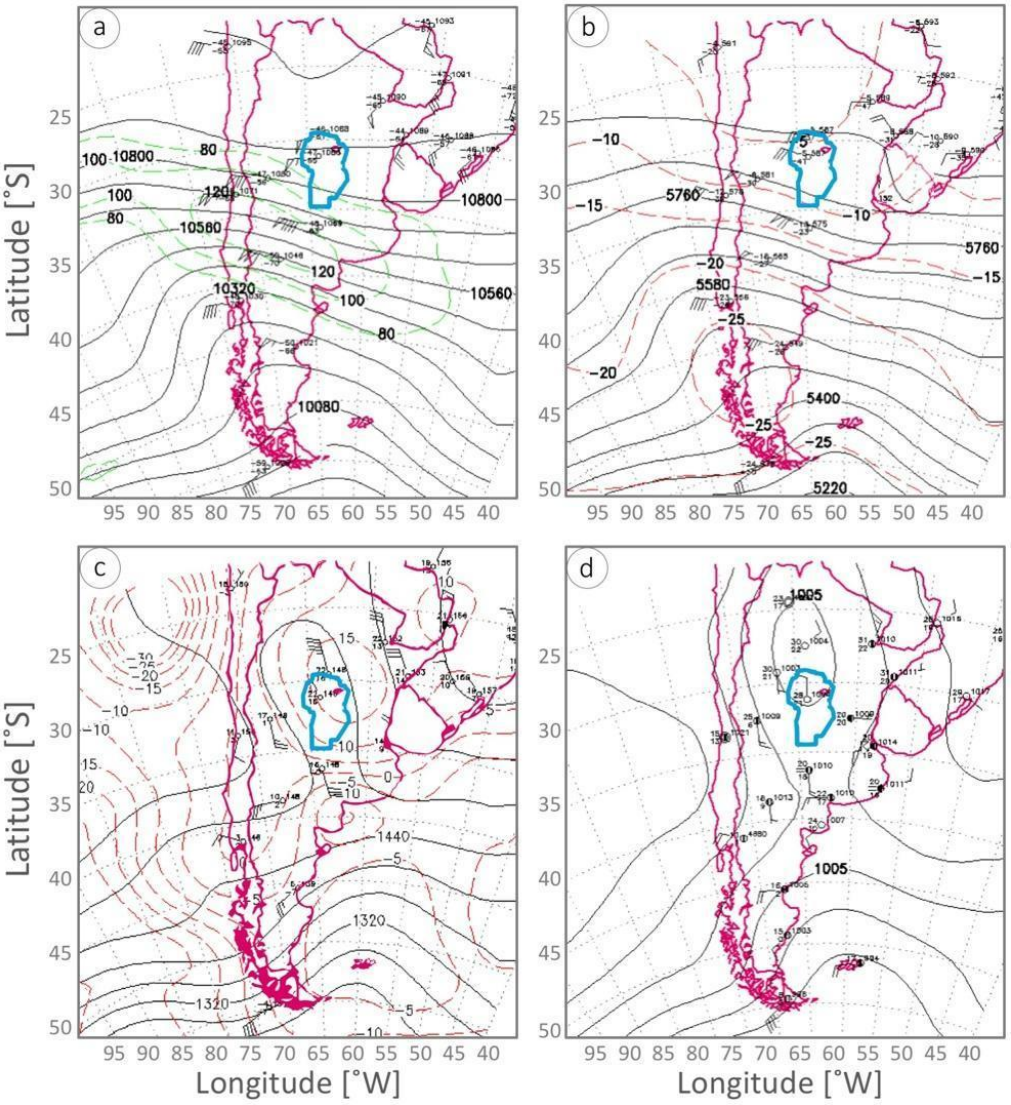

Fig. 2: Synoptic charts from 12 UTC on December 11, 2018 (a) isotachs (green) and geopotential (black) at 250 hPa, (b) temperature (red) and geopotential (black) at 500 hPa, (c) temperature (red) and geopotential (black) at 850 hPa, and (d) surface pressure (black). Wind barbs indicate wind information from each SMN radiosonde station at the corresponding pressure level and light blue contours denote Córdoba province.

Accepted

©2020 American Geophysical Union. All rights reserved.

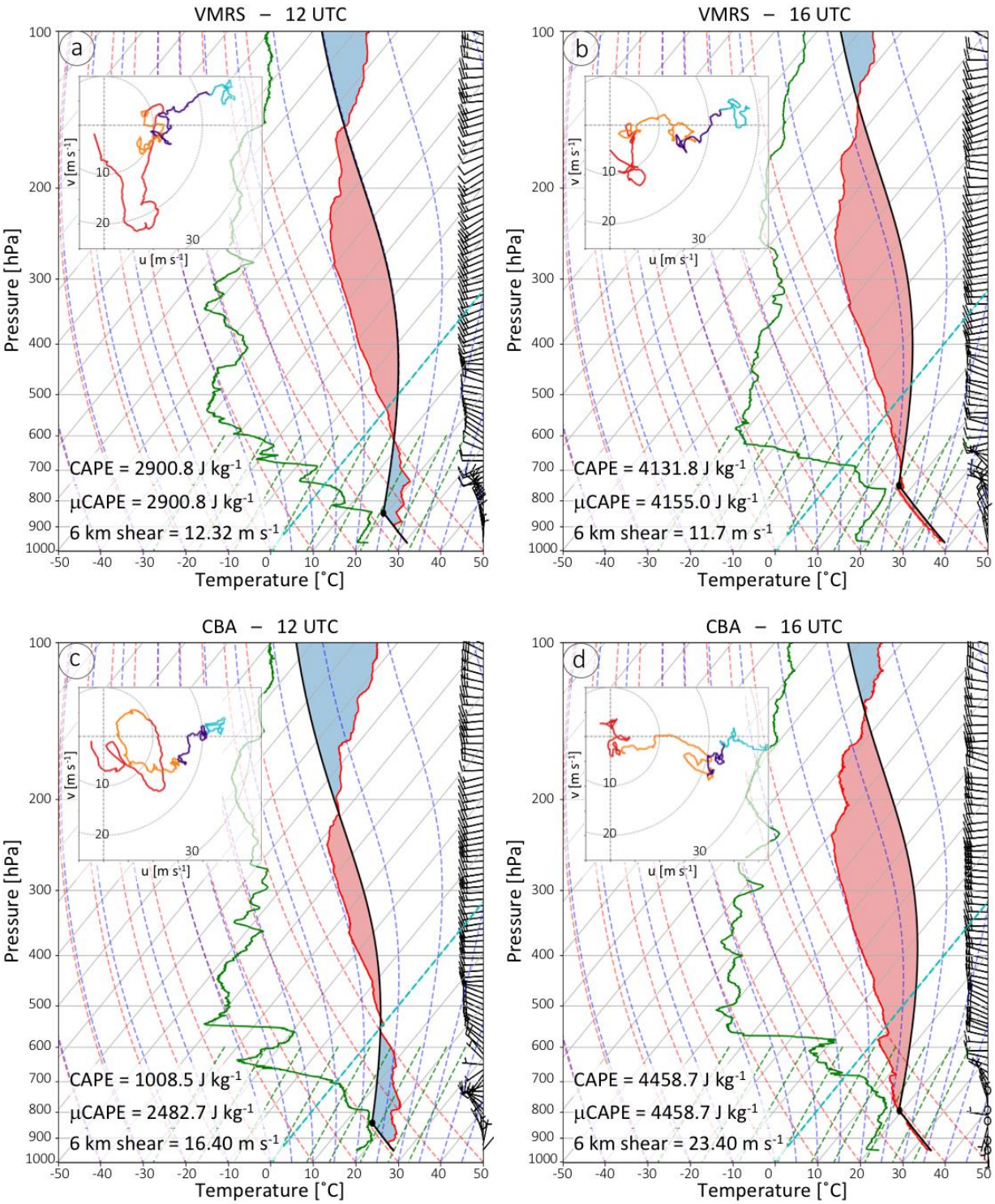

Fig. 3: Sondes from (a-b) Villa de María del Rio Seco – VMRS, and (c-d) Córdoba Airport – CBA. Sonde release time, shear between surface and 6 km height, CAPE, and μCAPE are indicated in each panel. Hodographs are color-coded by height of the sonde, red: surface-3 km, orange: 3-6 km, violet: 6-8 km, and blue: 8-10 km.

©2020 American Geophysical Union. All rights reserved.

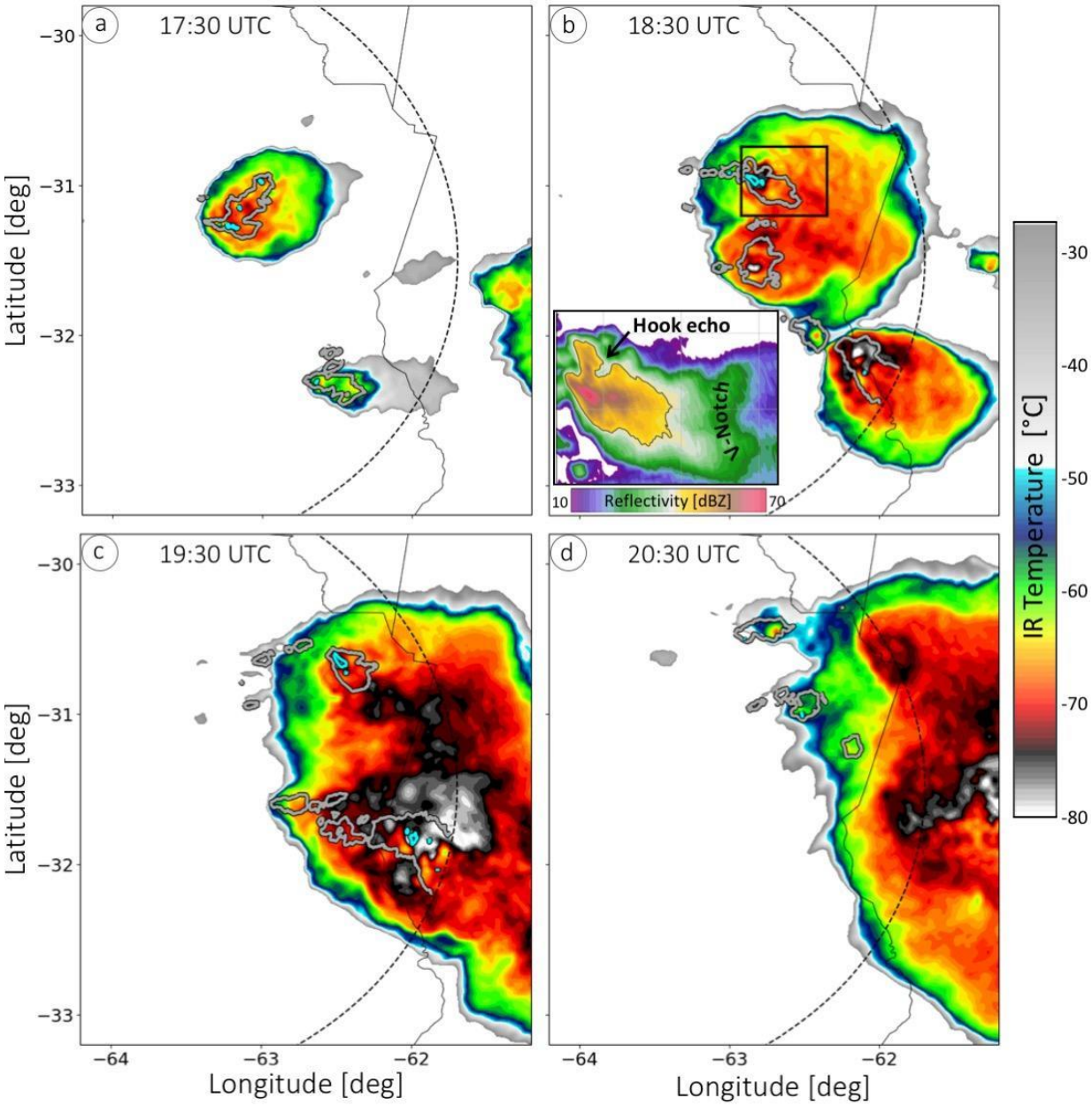

Fig. 4: Hourly observations from 17:30 UTC to 20:30 UTC (a-d) on Dec 11, 2018 of GOES-16 IR 10.3 brightness temperature (shaded) and 35, and 60 dBZ reflectivity at 1 km above ground (grey, and cyan contours respectively). RMA1 maximum range is indicated by dotted line. Reflectivity field at 0.5° elevation angle from the RMA1 at 18:30 UTC is also shown in (b).

Acce

©2020 American Geophysical Union. All rights reserved.

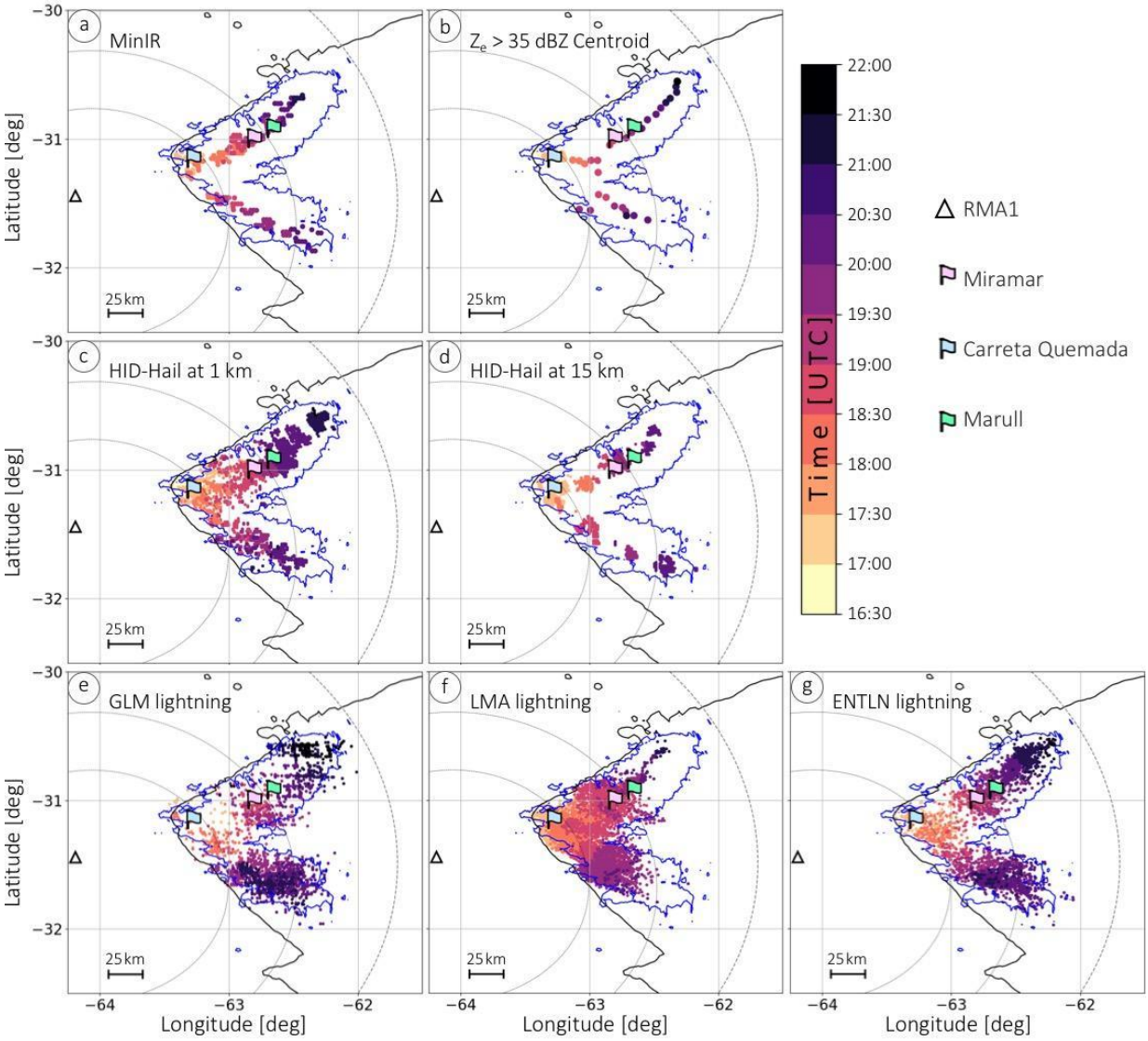

Fig. 5: Position of (a) observed MinIR, (b) 35-dBZ echo centroid at 1 km above ground, HID-retrieved hail at (c) 1 km, and (d) 15 km above ground, detected flashes from (e) GLM, (f) LMA, and (g) ENTLN. Observations are color-coded to correspond time in UTC. Location of RMA1 (triangle), locations where severe weather was reported (flags), RMA1 maximum radius (black dashed line), 100 and 150 km radius from LMA-center (black dotted lines), GOES-16 IR10.3 210 K integrated path (solid black line), and RMA1 35-dBZ integrated path (solid blue line) and km scale are shown in each panel.

Accepted

©2020 American Geophysical Union. All rights reserved.

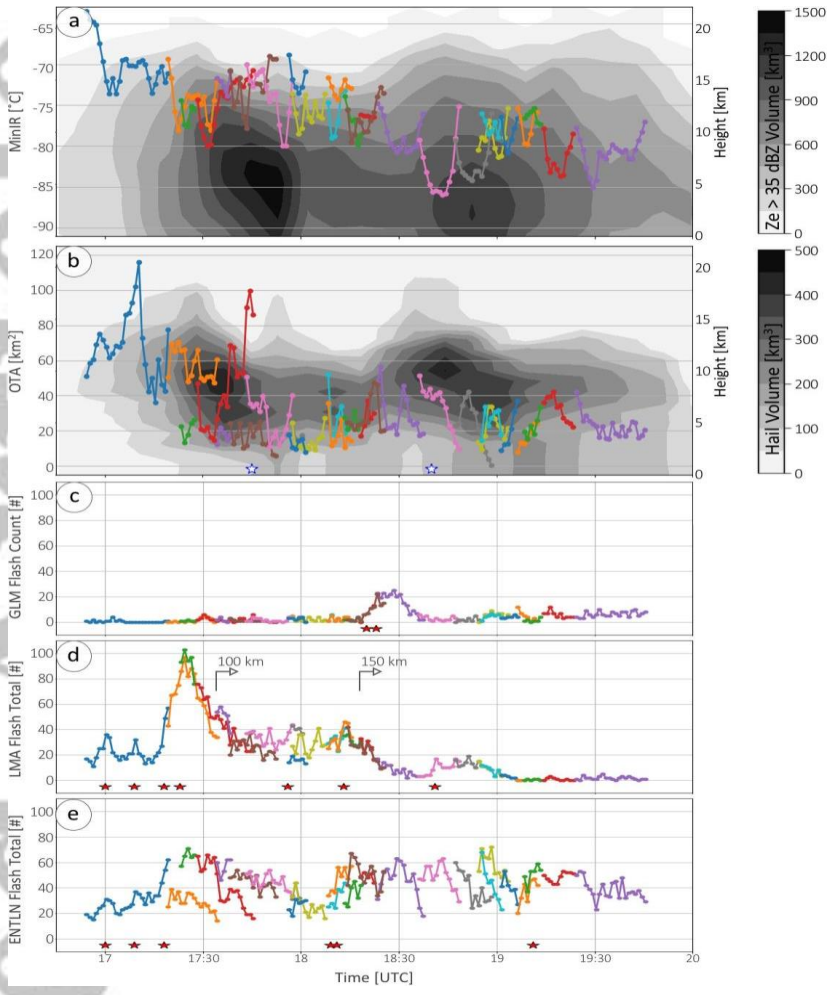

Fig. 6: Time evolution of (a) all tracked MinIR (lines) and volume covered with RMA1 observations with $Z_e \geq 35$ dBZ (shaded), (b) area associated with all tracked MinIR (OTA) (lines) and volume of HID-based hail (shaded), and flash counts from (c) GLM, (d) LMA, and (e) ENTLN. Each colored line corresponds to a tracked MinIR. Arrows denotes times when LMA-detected lightnings occurred 100 km and 150 km away from the LMA center. Red stars denote timing of LJ and blue star timing of hail observed at surface.

©2020 American Geophysical Union. All rights reserved.

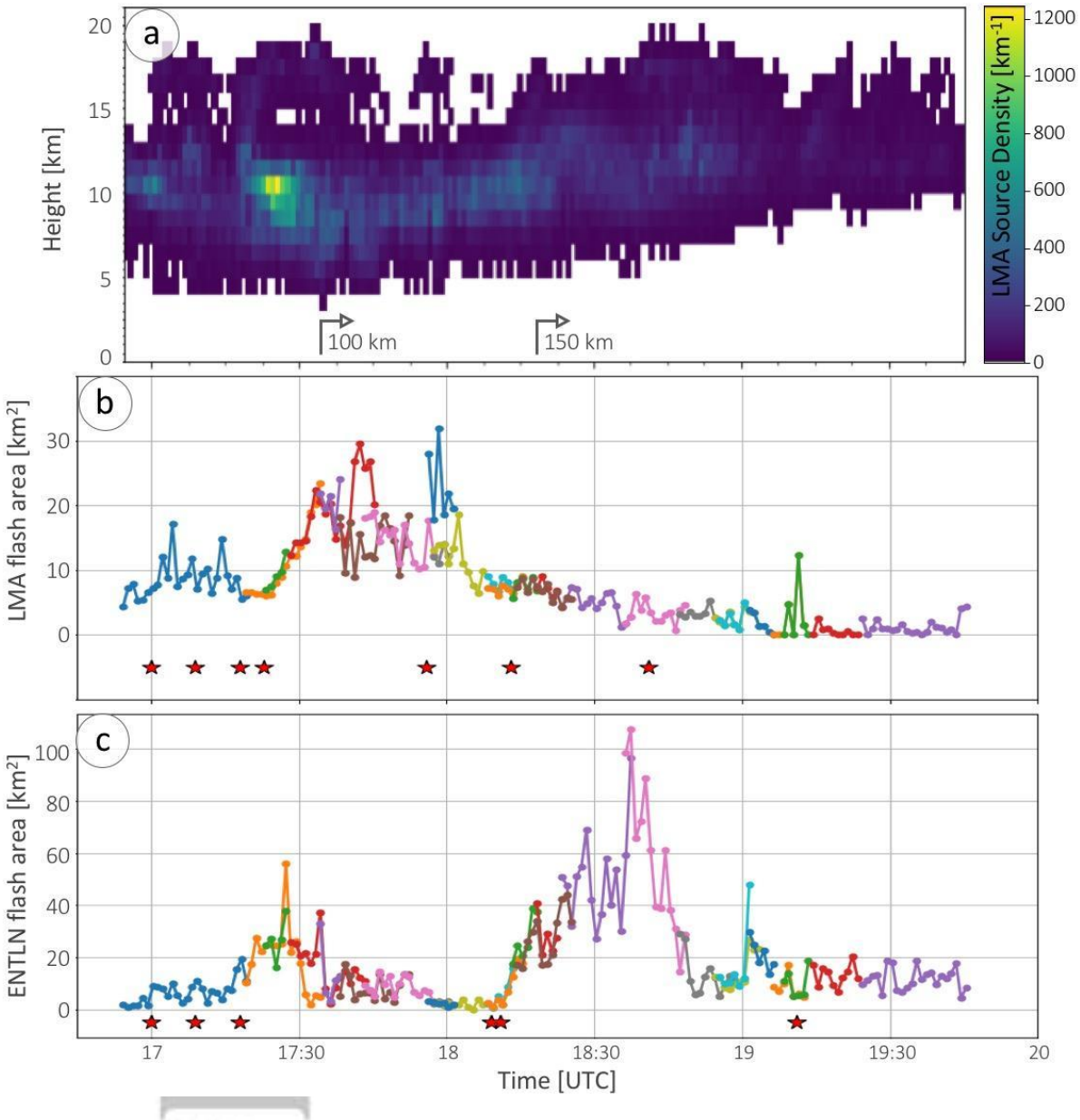

Fig. 7: Time evolution of (a) LMA source density as a function of height, (b) LMA flash area, and (c) ENTLN flash area. Colors in panels (b) and (c) denotes all the tracked MinIR. Stars denote timing of LJ. Each colored line corresponds to a tracked MinIR. Arrows in denote times when LMA-detected lightning occurred 100 km and 150 km away from the LMA center.

Accepted

©2020 American Geophysical Union. All rights reserved.

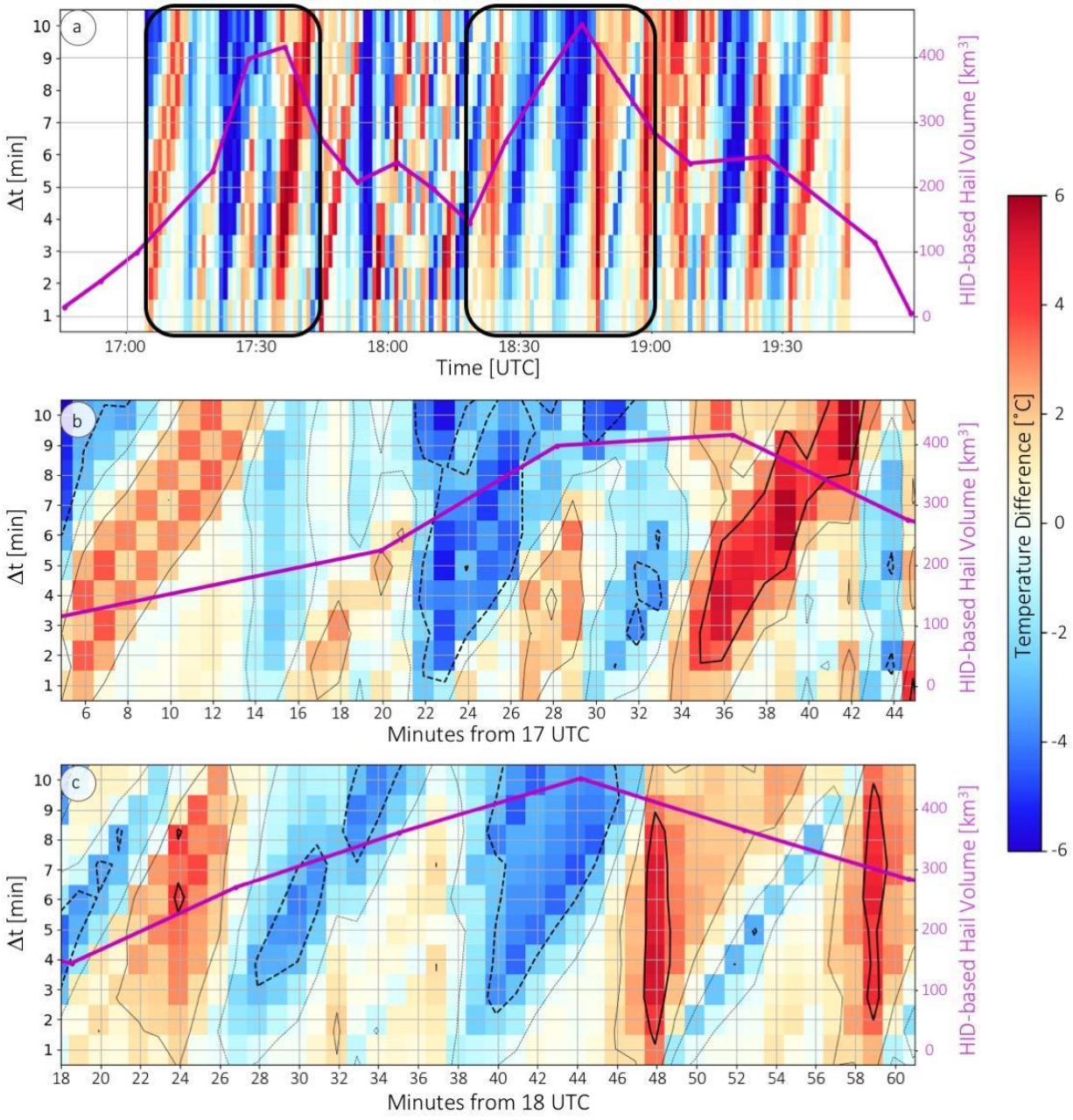

Fig. 8: Temporal evolution of HID-derived hail at 10 km (purple line) and MinIR trends as a function of the different temporal intervals used to compute the trend (from 1 to 10 minutes) and time (a) from 17 UTC to 20 UTC on December 11, 2018 and zoomed-in periods (b) from 17:05 UTC to 17:45 UTC and from (c) 18:18 UTC to 19:01 UTC. Black rectangles in (a) denote the zoomed-in times presented in panels (b) and (c).

©2020 American Geophysical Union. All rights reserved.